frontiers | Frontiers in Remote Sensing

ORIGINAL RESEARCH
published: 13 May 2022
doi: 10.3389/frsen.2022.885332

Polarimeter + Lidar–Derived Aerosol Particle Number Concentration

Joseph S. Schlosser[1], Snorre Stamnes[2], Sharon P. Burton[2], Brian Cairns[3], Ewan Crosbie[2,4], Bastiaan Van Diedenhoven[5], Glenn Diskin[2], Sanja Dmitrovic[6], Richard Ferrare[2], Johnathan W. Hair[2], Chris A. Hostetler[2], Yongxiang Hu[2], Xu Liu[2], Richard H. Moore[2], Taylor Shingler[2], Michael A. Shook[2], Kenneth Lee Thornhill[2,4], Edward Winstead[2,4], Luke Ziemba[2] and Armin Sorooshian[1,6,7]**

[1]University of Arizona, Department of Chemical and Environmental Engineering, Tucson, AZ, United States, [2]NASA Langley Research Center, Hampton, VA, United States, [3]NASA Goddard Institute for Space Studies, New York, NY, United States, [4]Science Systems and Applications, Inc., Lanham, MD, United States, [5]Netherlands Institute for Space Research, Utrecht, Netherlands, [6]University of Arizona, James C. Wyant College of Optical Sciences, Tucson, AZ, United States, [7]University of Arizona, Department of Hydrology and Atmospheric Sciences, Tucson, AZ, United States

OPEN ACCESS

Edited by:
Qiangqiang Yuan,
Wuhan University, China

Reviewed by:
Weizhen Hou,
Aerospace Information Research Institute (CAS), China
Xiaoguang Xu,
University of Maryland, United States

***Correspondence:**
Snorre Stamnes
snorre.a.stamnes@nasa.gov
Armin Sorooshian
armin@arizona.edu

Specialty section:
This article was submitted to Satellite Missions, a section of the journal Frontiers in Remote Sensing

Received: *28 February 2022*
Accepted: *11 April 2022*
Published: *13 May 2022*

Citation:
Schlosser JS, Stamnes S, Burton SP, Cairns B, Crosbie E, Van Diedenhoven B, Diskin G, Dmitrovic S, Ferrare R, Hair JW, Hostetler CA, Hu Y, Liu X, Moore RH, Shingler T, Shook MA, Thornhill KL, Winstead E, Ziemba L and Sorooshian A (2022) Polarimeter + Lidar–Derived Aerosol Particle Number Concentration. Front. Remote Sens. 3:885332. doi: 10.3389/frsen.2022.885332

In this study, we propose a simple method to derive vertically resolved aerosol particle number concentration (N_a) using combined polarimetric and lidar remote sensing observations. This method relies on accurate polarimeter retrievals of the fine-mode column-averaged aerosol particle extinction cross section and accurate lidar measurements of vertically resolved aerosol particle extinction coefficient such as those provided by multiwavelength high spectral resolution lidar. We compare the resulting lidar + polarimeter vertically resolved N_a product to *in situ* N_a data collected by airborne instruments during the NASA aerosol cloud meteorology interactions over the western Atlantic experiment (ACTIVATE). Based on all 35 joint ACTIVATE flights in 2020, we find a total of 32 collocated *in situ* and remote sensing profiles that occur on 11 separate days, which contain a total of 322 cloud-free vertically resolved altitude bins of 150 m resolution. We demonstrate that the lidar + polarimeter N_a agrees to within 106% for 90% of the 322 vertically resolved points. We also demonstrate similar agreement to within 121% for the polarimeter-derived column-averaged N_a. We find that the range-normalized mean absolute deviation (NMAD) for the polarimeter-derived column-averaged N_a is 21%, and the NMAD for the lidar + polarimeter-derived vertically resolved N_a is 16%. Taken together, these findings suggest that the error in the polarimeter-only column-averaged N_a and the lidar + polarimeter vertically resolved N_a are of similar magnitude and represent a significant improvement upon current remote sensing estimates of N_a.

Keywords: RSP, HSRL-2, column-averaged Na, vertically resolved Na, AOD, ACTIVATE, EVS-3, aerosol

1 INTRODUCTION

Aerosol particle number concentration (N_a) is an important aerosol microphysical property for many applications including air quality and aerosol–cloud interactions. Historically, N_a has been difficult to retrieve from remote sensing measurements that are sensitive to the aerosol scattering cross section, which scales with N_a to the first power and particle diameter (D) to a higher power. Thus, uncertainty in the aerosol size distribution translates directly into a much greater uncertainty in the retrieved N_a than would be the case when trying to retrieve the higher order moments of the aerosol population (e.g., surface area and volume) (Knobelspiesse et al., 2011; Georgoulias et al., 2020). While still limited to optically-active particles (i.e., D $\gtrsim$ 150 nm), the combination of next-generation polarimeter and lidar measurements makes the retrieval of N_a possible. First, multi-angle, multichannel polarimeter observations, such as those from the research scanning polarimeter (RSP), allow for accurate retrieval of column-averaged fine- and coarse-mode aerosol properties (Cairns et al., 1999; Stamnes et al., 2018). Second, multiwavelength high spectral resolution lidar (HSRL-2) measurements provide accurate, vertically resolved measurements of aerosol extinction and depolarization (Hair et al., 2008). The HSRL-2 observations also provide accurate (within ~30 m) retrieval of the mixed layer height (MLH, Scarino et al., 2014).

A previous study demonstrated a median relative bias between HSRL-2 lidar- and in situ–derived N_a of 33% and 47%; the lidar-derived N_a was retrieved by inverting HSRL-2–only aerosol products to produce vertically resolved N_a (Sawamura et al., 2017; Müller et al., 2019). In this study, we demonstrate a simple yet powerful method that uses combined lidar and polarimeter aerosol products to derive vertically resolved N_a in the troposphere that has a median relative bias of 30%. This lidar + polarimeter method has the benefit of being able to rapidly take advantage of column-averaged fine-mode aerosol cross section retrieved by polarimeters such as the RSP and collocated lidar measurements of aerosol extinction coefficient at 532 nm from HSRL lidar such as the HSRL-2 and HSRL-1. However, the two approaches are complementary, particularly since HSRL-2–type lidar with an added 355 nm channel are capable of retrieving the vertically resolved aerosol effective radius, which is one of the main parameters that determines the aerosol extinction cross section, and can be used together with the column-averaged fine- and coarse-mode effective radii retrieved by polarimeters such as RSP to correct the column-averaged aerosol extinction cross section for vertical changes due to changes in aerosol size. Since the lidar + polarimeter method presented in this study requires only profiles of the extinction coefficient at 532 nm, it can be readily applied to lidar + polarimeter data sets that have high spectral resolution capability at 532 nm, such as the NASA airborne HSRL-1 and HSRL-2 lidar, and the HSRL-1–type lidar system that will be onboard the future NASA atmosphere observing system (AOS) mission that is expected to launch by 2030.

Both aerosol index (AI) and aerosol optical depth (AOD) are commonly used as proxies for vertically variable cloud condensation nuclei (CCN) concentrations to quantify aerosol–cloud interactions, but there are limitations to using such proxies. The aerosol index convolves the N_a, size, single-scattering albedo, and complex refractive index into one number, and the accurate retrieval of AI can be subject to accuracy issues depending on which wavelengths are used (Buchard et al., 2015; Hammer et al., 2016). Furthermore, the relationships between AOD (or AI) and cloud drop number concentration (N_d) in pre-industrial and present-day conditions are different, whereas the relationship between CCN and N_d is similar in both of these periods (Gryspeerdt et al., 2017; Grosvenor et al., 2018). It is therefore highly desirable to use observational data to retrieve an aerosol proxy that is as close to CCN as possible since such relationships are expected to be more robust than those using more distant proxies such as AOD and AI (Shinozuka et al., 2015; Hasekamp et al., 2019). A significantly more direct proxy for CCN is the vertically resolved accumulation mode N_a.

There have only been a limited number of aerosol–cloud interaction studies that are historically focused on the western North Atlantic N_a (Sorooshian et al., 2020), but its gradients of low to high aerosol number concentrations provide an excellent environment to demonstrate the capability to remotely sense N_a (Quinn et al., 2019; Dadashazar et al., 2021b,a). For the majority of the year, the western North Atlantic's persistent cloud cover, only temporarily interspersed with clear-sky conditions of broken cloud fields, makes passive remote sensing measurements of aerosol properties in this region very challenging (Feingold, 2003; Braun et al., 2021; Painemal et al., 2021). Methods to process polarimeter and lidar data that perform well across the extreme situations encountered in the western North Atlantic may be expected to work well globally. For this study, we use measurements from the first two deployments of ACTIVATE in 2020.

The first and second ACTIVATE deployments were carried out from 14 February to 12 March 2020 and from 13 August to 30 September 20, respectively. ACTIVATE features a unique data set collected during 35 joint science flights with two aircraft flying in synchronous flight patterns (Sorooshian et al., 2019). One of the two ACTIVATE aircraft, a Beechcraft King Air, was collecting remote sensing data (i.e., lidar and polarimetry) while flying at high altitudes between 8 and 9 km. Simultaneously, the second aircraft, a HU-25 Falcon, was collecting *in situ* data while operating between the ocean surface and the top of the PBL. Throughout ACTIVATE, these two aircraft operated with close spatiotemporal proximity (within 6 min and 15 km) to each other whenever possible.

The experimental design and study region of ACTIVATE offer an ideal opportunity to evaluate the reliability of the novel vertically resolved N_a developed in this work. First, in **Section 2**, we present the instrumentation and corresponding measurements used from the each of the two aircraft to both produce and validate vertically resolved N_a. In **Section 2** we also present the formulation for deriving vertically resolved N_a from 1) column-averaged fine- and coarse-mode aerosol particle extinction cross section (σ_{ext}) from the polarimeter and 2) the total aerosol particle extinction coefficient (α_{ext}) from the lidar. Next, we describe the processing of the *in situ* data that we use to validate the novel N_a product presented in this work. After describing the data processing and collocation methods, we show results of the *in situ* validation of this novel vertically resolved N_a performed using case studies that have acceptable collocation and environmental conditions in **Section 3**. Our conclusions for this method are summarized in **Section 4**.

2 METHODOLOGY

A glossary of all acronyms and symbols used in this study is provided in **Table 1**.

TABLE 1 | Definition of acronyms, variables, and optional subscripts used to mark mode-specific parameters in alphabetical order.

Acronym	Definition
ACTIVATE	Aerosol Cloud meTeorology Interactions oVer the western ATlantic Experiment
AI	Aerosol index
AOD	Aerosol optical depth
AOS	Atmosphere observing system
ATH	Aerosol top height
CCN	Cloud condensation nuclei
CDP	Cloud droplet probe
DLH	Diode laser hygrometer
HSRL-2	Multiwavelength high spectral resolution lidar
LAS	Laser aerosol spectrometer
LDR	Linear depolarization ratio
LWC	Liquid water content
MLH	Mixed layer height
NMAD	Range-normalized mean absolute deviation
NRMSD	Range-normalized root-mean-square deviation
PBL	Planetary boundary layer
RH	Relative humidity
RSP	Research scanning polarimeter
Variable	Definition
α_{ext}	Aerosol particle extinction coefficient
D	Particle diameter
n_p	Number of points used for comparison
N_a	Aerosol particle number concentration
N_{RSP}	Column-averaged aerosol particle number concentration derived from the RSP data
$N_{\mathrm{HSRL+RSP}}$	Vertically resolved aerosol particle number concentration derived from HSRL and RSP data
N_{LAS}	Aerosol particle number concentration of particles with dry optical diameters between 94 and 3,488 nm
N_{CDP}	Number concentration of particles with ambient optical diameters between 2000 and 50,000 nm
N_d	Cloud drop number concentration
p-value	Probability that the two parameters are not correlated (i.e., probability that the null-hypothesis is true)
P_{75}	75th *percentile*
P_{90}	90th *percentile*
r	Correlation coefficient
r_e	Aerosol particle size distribution effective radius
$r_{e,94\text{–}1130}$	Effective radius of the particles that have dry optical diameters between 94 and 1,130 nm
σ_{ext}	Aerosol particle extinction cross section
Subscript	Definition
f	Parameter is specific to the fine mode of aerosol particle size distribution
c	Parameter is specific to the coarse mode of aerosol particle size distribution

2.1 Study Region Description

Figure 1 demonstrates the spatial coverage that was observed during the first two deployments of ACTIVATE. The ACTIVATE study region is characterized as predominately a marine environment impacted by anthropogenic continental outflow (Corral et al., 2021; Painemal et al., 2021). In most marine conditions the coarse-mode aerosol concentrations are composed primarily of sea salt, which accounts for a small percentage of the N_a in the troposphere (Murphy et al., 2019). This is especially true when the marine background is influenced by anthropogenic continental outflow where total N_a can be on the order of 1,000 cm^{-3}.

2.2 Measurement Summary

A list of instruments and corresponding measurements utilized from each of the ACTIVATE aircraft is provided in **Table 2**. The RSP aerosol product is based on an optimal estimate using the research scanning polarimeter–microphysical aerosol properties from polarimetery (RSP-MAPP) algorithm (Stamnes et al., 2018). Fine- and coarse-mode aerosol optical and microphysical properties are directly retrieved using seven channels that measure the total and polarized radiance across the visible–shortwave spectrum (wavelength = 410–2,260 nm) with over 100 viewing angles between ±55°. The RSP has a field of view of 14 mrad, which results in a ~126 m footprint for an aircraft at 9 km altitude. This RSP retrieval uses a coupled atmosphere–ocean radiative transfer model to improve the accuracy of the retrieved aerosol properties.

The RSP-MAPP retrieval algorithm (v1.48) inverts RSP data under the assumption that the aerosols are bimodal, split into a fine-mode and coarse-mode aerosol, with each mode defined by a lognormal size distribution. This version of RSP-MAPP assumes that the aerosol size distribution has one fine-mode and one coarse-mode comprising non-absorbing sea salt particles. Such a

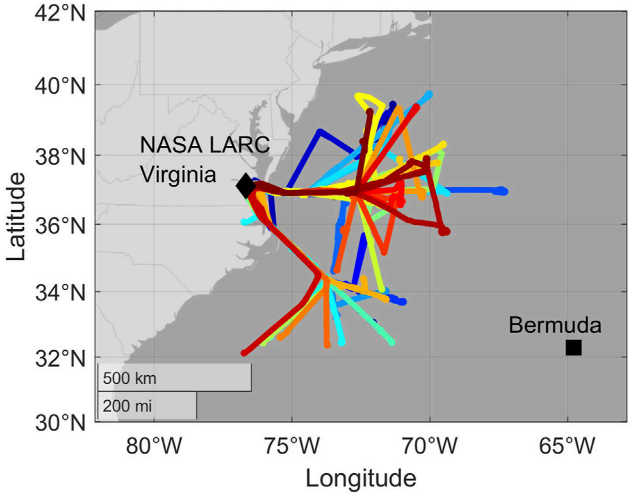

FIGURE 1 | Flight tracks from the 35 two-aircraft research flights that were carried out during the first two deployments of ACTIVATE in the winter and summer of 2020. Each flight track color corresponds to a different ACTIVATE research flight.

bimodal aerosol model works well over the ocean because the RSP visible to shortwave-infrared channels are not sensitive to particles D $\lesssim$ 100 nm. The fine-mode aerosol properties including aerosol absorption are fully retrieved, namely, fine-mode AOD, size distribution parameters of effective radius and effective variance, and complex refractive index. The coarse-mode AOD, effective radius, and effective variance are also retrieved under the assumption that the coarse-mode consists of non-absorbing sea salt particles with a real refractive index close to water. The coarse-mode sea salt aerosol is assumed to be located from the ocean surface to 1 km, while the fine-mode aerosol is assumed to be mixed homogeneously from the ocean surface to the aerosol top height, which is also retrieved. From the aerosol optical and microphysical properties, RSP-MAPP implicitly retrieves the column-averaged fine- and coarse-mode σ_{ext} ($\sigma_{\mathrm{ext},f}$ and $\sigma_{\mathrm{ext},c}$, respectively). The RSP-MAPP algorithm also provides an estimate of fine- and coarse-mode column-averaged N_a ($N_{a,f}$ and $N_{a,c}$, respectively). In cloud-free conditions, RSP and HSRL-2 column AODs have been shown to agree to within 0.02 at 532 nm (Stamnes et al., 2018). The column-averaged aerosol particle number concentration derived from the RSP data (N_{RSP}) is defined as the following:

$$N_{\mathrm{RSP}} = \bar{N}_a = \frac{\mathrm{AOD}}{\bar{\sigma}_{\mathrm{ext}} \times \mathrm{ATH}}, \tag{1}$$

where we explicitly use a bar to represent the *column-averaged* polarimeter-retrieved aerosol cross section and number concentration. The AOD and σ_{ext} are referenced at 532 nm. Both AOD and N_{RSP} are, in part, governed by a retrieval of the aerosol top height (ATH, Wu et al., 2016). RSP-MAPP retrieves the ATH under the assumption that the fine-mode size and composition are uniform throughout the column, and as a result the fine-mode σ_{ext} is implicitly retrieved as a uniform value.

The HSRL-2 products include ambient vertically resolved lidar backscattering and extinction coefficients and ambient linear depolarization ratio (LDR) at wavelengths of 355, 532, and 1,064 nm (Fernald, 1984; Hair et al., 2008; Burton et al., 2018). The HSRL-2 field of view is 1 mrad, which corresponds to a ~9 m footprint for an aircraft at 9 km altitude. Similar to the RSP, the HSRL-2 is not very sensitive to particles that fall in or below the Aitken size range (Burton et al., 2016). The HSRL-2 can also provide AOD by using the difference in the molecular channel signals at the top and bottom of the layer. Finally, the HSRL-2 retrieves the MLH (Scarino et al., 2014). To limit the scope of this analysis to spherical particles, LDR is used to filter out non-spherical from the data set (Burton et al., 2013). A LDR threshold of > 13% was used to filter out non-spherical particles from the analysis. This LDR threshold was chosen because the ACTIVATE study region is characterized as predominately a marine environment impacted by anthropogenic continental outflow (Corral et al., 2021; Painemal et al., 2021).

The measured *in situ* N_a values are used for the validation of the N_a product presented in this work. These data are taken from the laser aerosol spectrometer (LAS, Model 3,340, TSI, Inc.), which measures concentrations of particles with dry D ranging in sizes from 94 to 7,500 nm at a 1 Hz temporal resolution. The N_a measurements provided by the LAS are provided at standard temperature and pressures (273.15 K and 1,013 mb). While the LAS has a measurement range up to 7,500 nm, the maximum cutoff D of the sample inlet prevents the measurement of particles with ambient D greater than 5,000 nm (McNaughton et al., 2007; Chen et al., 2011). To take into account potential hygroscopic effects, we only include particles with dry optical D up to 3,488 nm in this analysis. The total N_a measured by the LAS is referred to from this point forward as N_{LAS}. The lower dry D cutoff of 94 nm is similar to the lower cutoff of the remotely-

TABLE 2 | List of measurement products used in this study, which are grouped by the both the instrument each measurement was derived from and the ACTIVATE aircraft each instrument was mounted on.

Aircraft	Instrument	Aerosol property
King Air	HSRL-2	Vertically resolved α_{ext} at 532 nm, vertically resolved LDR at 532 nm, total AOD at 532 nm, and MLH
King Air	RSP	Fine- and coarse-mode AOD at 532 nm, column-averaged $\sigma_{\mathrm{ext},f}$ at 532 nm, column-averaged $N_{a,f}$, and ATH
Falcon	LAS	N_{LAS} and $r_{e,94\text{–}1130}$
Falcon	DLH	RH
Falcon	CDP	LWC and N_d (i.e., N_{CDP})

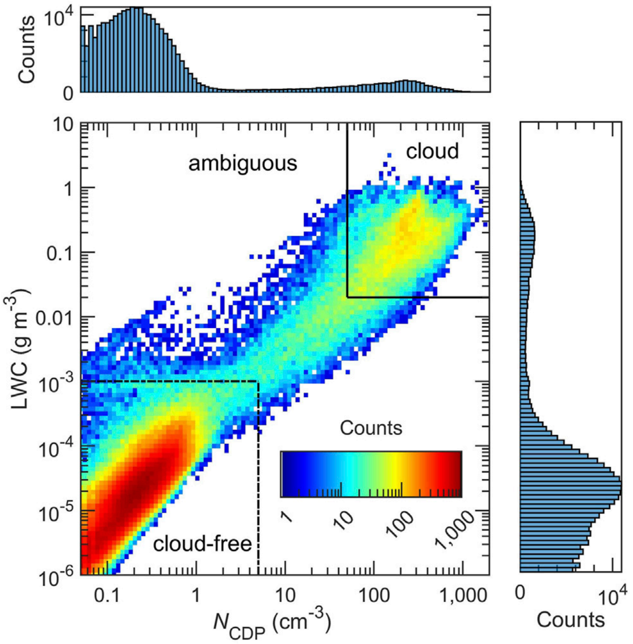

FIGURE 2 | Log-log heat map of liquid water content (LWC) and cloud drop number concentration (N_d) with corresponding marginal semi-log histograms generated using all available 1 *Hz* cloud droplet probe (CDP) data measured during ACTIVATE 2020. The number of points used for comparison (n_p) on each panel is 465, 292. Points on the heat map that are classified as cloud-free have LWC and N_d values that are below horizontal (at 0.001 $g\ m^{-3}$) and vertical (at 5 cm^{-3}) dashed-black lines, respectively. Points on the heat map that are classified as cloud have LWC and N_d values that are above the horizontal (at 0.02 $g\ m^{-3}$) and vertical (at 50 cm^{-3}) solid-black lines, respectively. Points on the heat map that fall outside of the cloud or the cloud-free classifications are classified as ambiguous.

sensed N_a values but the N_{LAS} unavoidably misses some of the coarse-mode N_a due to the aforementioned inlet limitations.

The LAS has a low counting efficiency at three low size bins: 94–106 nm, 106–119 nm, and 119–133 nm, which we compensate for by multiplying the number concentration measured in those size ranges by correction factors of 1.90, 1.45, and 1.20, respectively. Losses for the LAS are calculated at nominal cabin temperature (20 °C) and pressure for low-altitude flight segments (900 mb). These correction factors are calculated using the product of losses by impaction, gravitational settling, and diffusion (Baron and Willeke, 2011). All tubing is conductive silicone and flows are laminar from the inlet manifold to both the LAS optical block. In addition to N_{LAS}, the aerosol particle size distribution effective radius (r_e) of the fine-mode is derived from the corrected LAS and defined as effective radius of the particles that have dry optical diameters between 94 and 1,130 nm ($r_{e,94-1130}$). The $r_{e,94-1130}$ is used primarily to assess the homogeneity of the fine-mode aerosol particles that is assumed to be true for the RSP-MAPP–derived fine-mode σ_{ext}.

Ambient liquid water content (LWC) and N_d are used to classify *in situ* data as cloud-free, ambiguous, or cloud. Ambient LWC and N_d are both derived from ambient particle size distribution measured by using a cloud droplet probe (CDP, Droplet Measurement Technologies, Sinclair et al., 2019). The CDP can measure particles in the ambient D size range of 2,000–50,000 nm, and the N_d-CDP derived by the CDP is noted by N_{CDP}. An important limitation with deriving LWC from the CDP is an integration of the particle size distribution assuming unit density and constrained to the real refractive index of water. If the particles are anything other than spherical, with unit density and with real refractive index of 1.33, this LWC number has no meaning. Previous studies of aerosol–cloud interactions in marine environments have used a LWC threshold of < 0.02 g m^{-3} to classify data as cloud-free (Wang et al., 2014; Dadashazar et al., 2017; MacDonald et al., 2018). While this LWC threshold generally works well, the LWC of stratiform clouds has been shown to be as low as 0.0012 g m^{-3} (Yin et al., 2014). To ensure the avoidance of cloud edges, measurements where LWC was between 0.001 and 0.02 g m^{-3} and where N_d was between 5 and 50 cm^{-3} are classified as ambiguous. Only measurements where LWC and N_d were less than 0.001 g m^{-3} and 5 cm^{-3}, respectively, are classified as cloud-free.

To further illustrate the three cloud classifications (cloud-free, ambiguous, and cloud) used in this study, **Figure 2** provides a heat map (with marginal histograms) of all available 1 Hz LWC and N_{CDP} measurements taken during ACTIVATE 2020. In addition to the LWC and N_d thresholds, a sampling inlet flag is used to verify the Falcon aircraft's sampling inlet was sampling air *via* the isokinetic inlet or *via* the counterflow virtual impactor (BMI Inc.; Shingler et al., 2012). The former is used to sample aerosol particles, while the latter is used to sample cloud droplets. Finally, ambient relative humidity (RH) is derived from measurements of the water vapor mixing ratio, which is measured by using a diode laser hygrometer (DLH, Diskin et al., 2002), and of temperature, which is measured by using the turbulent air motion measurement system (TAMMS, Thornhill et al., 2003). Ambient RH is used for an indication of the impacts of water vapor on $r_{e,94-1130}$.

2.3 Deriving Vertically Resolved Aerosol Number Concentration

In this section, we describe the mathematical formulation used to derive N_a from standard HSRL-2 and RSP products. The formulation to derive N_a described in this study has its foundation in the spherical particle Mie theory (Bohren and Huffman, 1983). Using the Mie theory and the environmental setup established in **Section 2.1**, we describe how column-averaged $\sigma_{\mathrm{ext},f}$ (from RSP-MAPP) and vertically resolved α_{ext} (from HSRL-2) can be used to calculate vertically resolved N_a. We limit this analysis to the 532 nm wavelength for simplicity. While the RSP-derived σ_{ext} is a column average and is separated into fine- and coarse-modes, we assume the fine- and coarse-mode aerosols are externally mixed as two distinct aerosol types. This assumption allows us to calculate a mixed σ_{ext} using number concentration weighted averaging as follows:

$$\sigma_{\mathrm{ext}} \equiv \sigma_{\mathrm{ext}}(z) = \frac{N_{a,f}(z) \times \sigma_{\mathrm{ext},f}(z) + N_{a,c}(z) \times \sigma_{\mathrm{ext},c}(z)}{N_{a,f}(z) + N_{a,c}(z)}, \quad (2)$$

where we show explicitly the vertically resolved dependence on altitude z. Aerosol particle extinction cross section is related to N_a at every altitude layer by α_{ext} using the following:

$$N_a \equiv N_a(z) = N_{a,f}(z) + N_{a,c}(z) = \frac{\alpha_{\text{ext}}(z)}{\sigma_{\text{ext}}(z)} \equiv \frac{\alpha_{\text{ext}}}{\sigma_{\text{ext}}}. \tag{3}$$

However, we choose cases based on the HSRL-2 and *in situ* measurements where the coarse-mode α_{ext} has a minimal impact, and accordingly simplify the equation to remove the coarse-mode terms. By setting the $N_{a,c}$ and $\sigma_{\text{ext,c}}$ terms to zero we obtain the following relationship for the aerosol number concentration from **Eqs (2)**, **(3)**, resulting in the method proposed in this study:

$$N_a \equiv N_a(z) = N_{a,f}(z) \approxeq \frac{\alpha_{\text{ext}}(z)}{\bar{\sigma}_{\text{ext},f}} \equiv \frac{\alpha_{\text{ext}}}{\sigma_{\text{ext},f}}, \tag{4}$$

where **Equation (4)** is applied to every altitude bin of the vertically resolved α_{ext} measured by the lidar (HSRL-2), while $\sigma_{\text{ext},f}$ is set equal to the column-averaged value retrieved by the polarimeter (RSP). The $\sigma_{\text{ext},f}$ is dependent on only the fine-mode aerosol size and composition. That the fine-mode aerosol cross section is kept constant is an assumption that the fine-mode aerosol properties do not significantly differ from the column-averaged value in such a way that it significantly biases the retrieval of N_a. Another limitation related to this assumption is that both extinction cross section and extinction coefficient are expected to increase with increasing RH. Using an average cross section could cause $N_{\text{HSRL+RSP}}$ to biased high/low with an increase/decrease of ambient size.

2.4 Data Handling and Analysis

This section describes how remote sensing and *in situ* data are processed to apply the N_a derivation outlined in **Section 2.3**. First, we limit the application of the method to observations of spherical aerosol particles using the LDR threshold of $\leq 13\%$ to filter out non-spherical data points from the smoothed α_{ext} data. Next, the α_{ext} and LDR data are smoothed into temporal-altitude grids of 0.0167 Hz and 150 m. The HSRL-2–derived AOD are also smoothed to a temporal resolution of 0.0167 Hz. Once the HSRL-2–derived α_{ext} and AOD data are smoothed, they are then collocated with the RSP by comparing the timestamps and selecting the nearest HSRL-2 data point (in time) to each of the RSP data points. A total of 7,727 RSP data points are collocated with HSRL-2–derived AOD and vertically resolved profiles of α_{ext}. Once the remote sensing data are placed in the native RSP temporal resolution, any scenes where the HSRL-2- and RSP-derived AOD deviate from each other are discarded. Points are discarded when deviation between the two AOD measurements exceeds whichever is greater 0.05 or 50% of the HSRL-2–derived AOD. As an additional constraint the fine-mode AOD derived from the RSP must be within 0.10 of the HSRL-2 AOD. The HSRL-2- and RSP-derived AOD can deviate from each other when there are cirrus clouds above the King Air, when there is at least one aerosol layer above the King Air, or when there are one or more detached troposphere aerosol layers. As a result of this filtering step, there are 774 collocated data points removed from the total set of 7,727. This empirical method of cloud and multiple aerosol layer influence does not guarantee the removal of all such contamination. In the future, the N_a derivation can be upgraded to be applied to conditions where aerosols are present in one or more detached troposphere layer(s) and in the presence of significant amounts of non-spherical aerosol particles.

After the remote sensing data are aligned and filtered, the aerosol particle number concentration of particles with dry optical diameters between 94 and 3,488 nm (N_{LAS}) data are filtered for clouds and adjusted to ambient temperature and pressure for direct comparison with the remote sensing observations. From the cloud filtered ambient N_{LAS} data, all available *in situ* vertical profiles (e.g., spirals, in-line descents, and in-line ascents) are organized for collocation with the remote sensing data. For this collocation stage the remote sensing profiles are collocated with the *in situ* profiles. The nearest remote sensing profile within 6 min and 15 km to the start or end of the *in situ* profile is selected for comparison. After collocation, N_{LAS} from each *in situ* profile is averaged to the same altitude grid as the HSRL-2 data (i.e., altitude bins that are 150 m in depth and extend from 0 to 9 km).

With collocation performed, the HSRL-2 + RSP-derived N_a (i.e., $N_{\text{HSRL+RSP}}$) can be equivalently compared to the N_{LAS} at each altitude grid point of each collocated vertical profile. In order to validate the column-averaged N_a that is derived from the RSP (i.e., N_{RSP}), the column-averaged N_{LAS} is calculated by taking an arithmetic mean of the entire N_{LAS} profile. With this final step, both $N_{\text{HSRL+RSP}}$ and N_{RSP} can be equivalently quantitatively validated using vertically resolved N_{LAS} or column-averaged N_{LAS}, respectively. This study makes use of correlation coefficient (r), range-normalized root-mean-square deviation (NRMSD), range-normalized mean absolute deviation (NMAD), and relative bias, which have been previously used for quantitative validation of aerosol microphysical properties (Sawamura et al., 2017; Stamnes et al., 2018). Each of these statistical metrics has the following formulations:

$$r = \frac{\sum_{j=1}^{n_p}\left[(X(j) - \bar{X}) \times (Y(j) - \bar{Y})\right]}{\sum_{j=1}^{n_p}[X(j) - \bar{X}]^2 \times \sum_{j=1}^{n_p}[Y(j) - \bar{Y}]^2}, \tag{5}$$

$$\text{NRMSD} = \frac{100\%}{\max(X) - \min(X)} \times \sqrt{\frac{\sum_{j=1}^{n_p}[Y(j) - X(j)]^2}{n_p}}, \tag{6}$$

$$\text{NMAD} = \frac{100\%}{\max(X) - \min(X)} \times \frac{\sum_{j=1}^{n_p}|Y(j) - X(j)|}{n_p}, \tag{7}$$

$$\text{relative bias} = \frac{Y(j) - X(j)}{Y(j) + X(j)} \times 2 \times 100\%, \tag{8}$$

where X and Y are the set of in situ–derived N_a and remote sensing–derived N_a, respectively; n_p is the total number of points for each set; and $\bar{X}$ and $\bar{Y}$ are the mean of sets X and Y, respectively. This study also makes use of the *p*-value corresponding to each r.

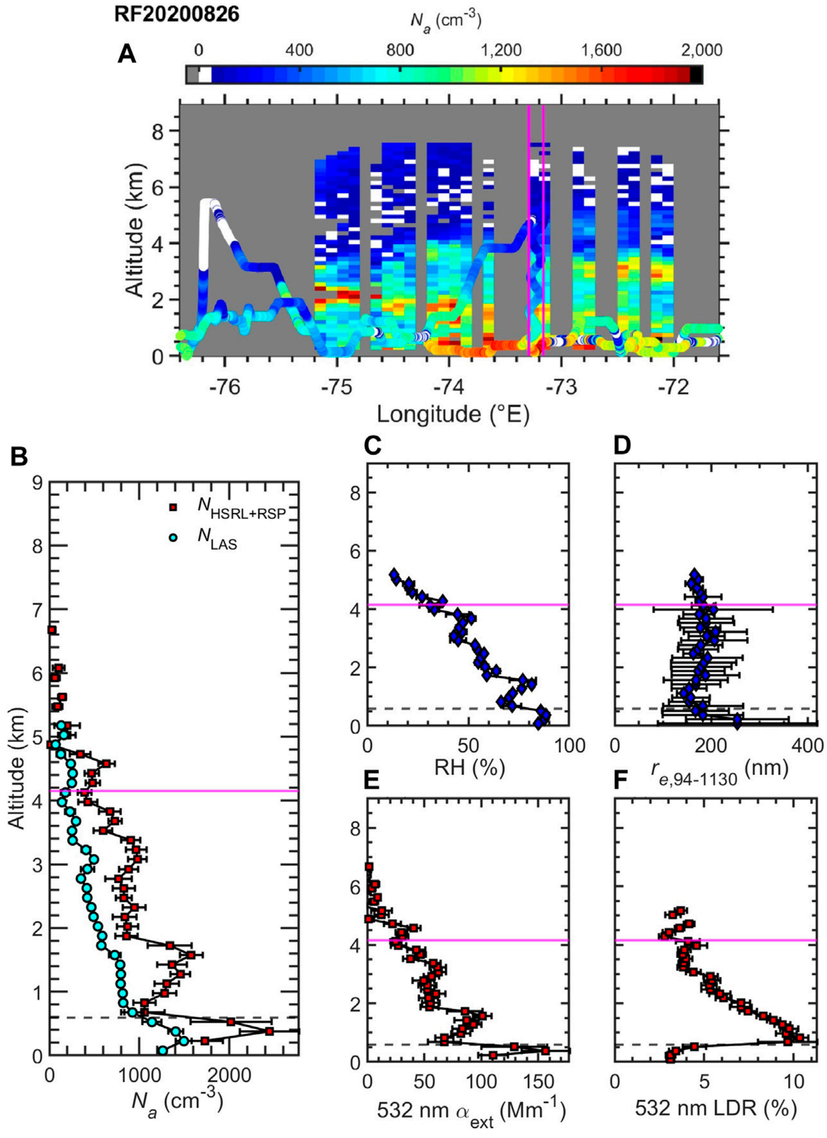

FIGURE 3 | Horizontal curtain **(A)** and vertical profiles **(B–F)** of remote sensing and *in situ* data gathered from the 'optimal' flight that occurred on 26 August 2020. The vertical profiles were taken from the *in situ* profile that occurred between 15:46:25 and 15:58:12 (UTC) on 26 August 2020. Panel **(A)** shows the flight track and surface plot colored by N_{LAS} and $N_{HSRL+RSP}$, respectively, where the magenta vertical lines mark the start and stop locations of the first optimal vertical *in situ* profile. Panel **(B)** show vertical profiles of average aerosol particle number concentration (derived from the various methods), **(C)** RH, **(D)** $r_{e,94-1130}$, **(E)** 532 nm α_{ext}, and **(F)** 532 nm LDR; where the whiskers mark ± one standard deviation. The horizontal dashed-black and solid-magenta lines mark the MLH and the ATH, respectively.

3 RESULTS

Out of the 35 two-aircraft flights in the first two deployments of ACTIVATE, there are a total of 42 full vertical profiles successfully collocated using the process described in **Section 2.4**. In order to be considered as an *in situ* vertical profile, each of these collocated profiles was required to have measurements across at least four altitude grid points. These 42 profiles are placed into three categories based on whether there are ambiguous- or cloud-flagged *in situ* data in the profile (see **Section 2.2**). The three classifications are described as follows: (1, *cloud-free profile*) vertical profiles where there are no *in situ* data flagged as ambiguous or cloud; (2, *ambiguous profile*) vertical profiles that have one or more *in situ* data point that is flagged as ambiguous but no points flagged as cloud; and (3, *cloud profile*) vertical profiles where at least one data point was classified as cloud. There are 32 profiles classified as cloud-free, two profiles classified as ambiguous, eight profiles classified as cloud of the profiles classified as cloud-free, and two profiles that featured extended spiral vertical profiles, which are fairly unusual for ACTIVATE, and targeted relatively high aerosol loading. These two "optimal" aerosol profiles extended to at least 5 km in altitude; hence, they offer an unprecedented

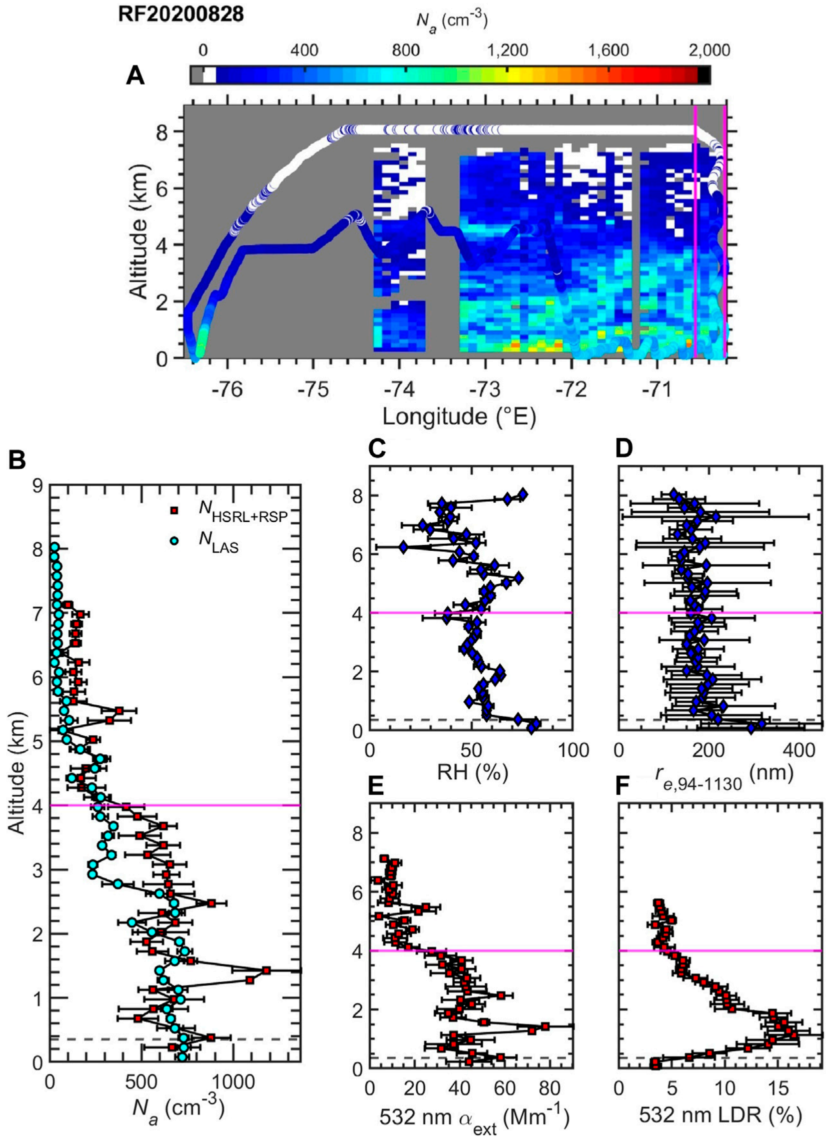

FIGURE 4 | Horizontal curtain **(A)** and vertical profiles **(B–F)** of remote sensing and *in situ* data gathered from the 'optimal' flight that occurred on 28 August 2020. The vertical profiles were taken from the *in situ* profile that occurred between 17:35:18 and 17:54:11 (UTC) on 28 August 2020. Panel **(A)** shows the flight track and surface plot colored by N_{LAS} and $N_{HSRL+RSP}$, respectively, where the magenta vertical lines mark the start and stop locations of the first optimal vertical *in situ* profile. Panel **(B)** show vertical profiles of average aerosol particle number concentration (derived from the various methods), **(C)** RH, **(D)** $r_{e,94\text{–}1130}$, **(E)** 532 nm α_{ext}, and **(F)** 532 nm LDR, where the whiskers mark ± one standard deviation. The horizontal dashed-black and solid-magenta lines mark the MLH and the ATH, respectively.

opportunity to validate the novel $N_{HSRL+RSP}$. In **Section 3.1** we analyze these two optimal profiles with more detail and show that the novel $N_{HSRL+RSP}$ has reasonable closure with N_{LAS}. Following this case study analysis, we analyze the entire *in situ* validation set in **Section 3.2**. These result demonstrated in this analysis warrant further study in future ACTIVATE deployments and other missions with combined lidar-polarimeter aerosol measurements.

3.1 Case Study of Optimal Aerosol Profiles

In this section, we examine the two optimal aerosol profiles from the first deployment of ACTIVATE 2020 (**Figures 3**, **4**). For these two profiles, each corresponding research flight took place in a generally cloud-free conditions (both low level and cirrus), that allow for the use of the novel $N_{HSRL+RSP}$ product to create altitude vs. longitude color maps of N_a to provide some spatial context to each profile (**Figure 3A**, **Figure 4A**). The $N_{HSRL+RSP}$ is gridded into 0.01° longitude bins (maintaining the 150 m altitude bins), but the *in situ* sampling flight track is displayed in the native 1 *Hz* resolution for qualitative, observational comparison of N_{LAS} and the $N_{HSRL+RSP}$. From this qualitative comparison, it is evident that the N_{LAS} and $N_{HSRL+RSP}$ reasonably agree for these two flights that include the optimal profiles. In addition to the qualitative comparison between N_{LAS} and $N_{HSRL+RSP}$, these vertically

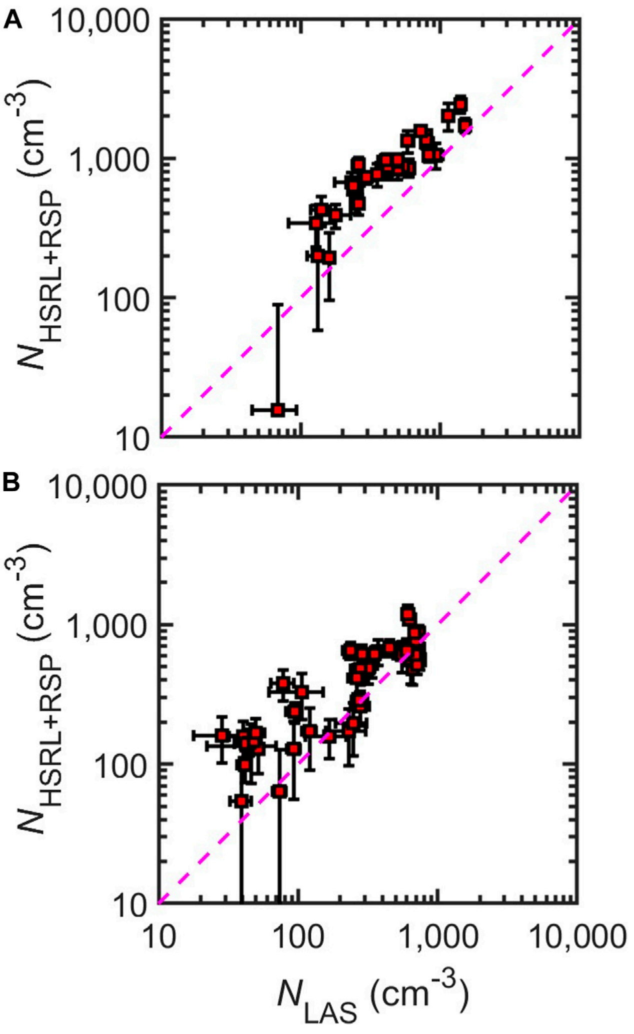

FIGURE 5 | Log-log plots of $N_{HSRL+RSP}$ versus N_{LAS} from **(A)** optimal *in situ* profile that occurred between 15:46:25 and 15:58:12 (UTC) on 26 August 2020 and **(B)** optimal *in situ* profile that occurred between 17:35:18 and 17:54:11 (UTC) on 28 August 2020. The goodness of fit statistics that correspond to panel **(A)** are r = 0.92, median relative bias = 64%, NMAD = 29%, NRMSD = 33%, and n_p = 34. The goodness of fit statistics for panel **(B)** are r = 0.81, median relative bias = 42%, NMAD = 21%, NRMSD = 28%, and n_p = 47.

resolved profiles illustrate the significant differences in the two profiles.

The first optimal profile's research flight occurred from 13:52:27 to 17:08:12 on 26 August 2020 (**Figure 3**). This first optimal flight appears to have had two aerosol layers, one below 1 km and one between 1 and 2 km (e.g., smoke aerosol), as well as N_{LAS} and $N_{HSRL+RSP}$ ranges that reached as high as 2,508 and 9,103 cm^{-3}, respectively. The second optimal flight occurred from 16:45:10 to 20:01:40 on 28 August 2020 (**Figure 4**) and had lower maximum N_{LAS} and $N_{HSRL+RSP}$ (1,031 and 4,209 cm^{-3}, respectively), relative to the first optimal flight. The second optimal profile's research flight had possibly more than one aerosol layer between 1 and 4 km, in addition to a homogeneous aerosol layer up to 1 km. Both of these profiles were observed to have detached aerosol layers above the PBL (e.g., smoke aerosol). Smoke aerosol was found to be present in this region on 26 August (Mardi et al., 2021) and on 28 August (Sorooshian et al., 2021).

Another contrast between the two optimal flight study regions was the MLH, which had the ranges of 0:00–0:88 km and 0:00–0:67 km for the first and second optimal flights, respectively. Both flights had similar RSP-ATH ranges that were 1:14–4:83 km and 1:83–4:85 km for the first and second optimal flights, respectively. In order to better analyze the closure between N_{LAS} and $N_{HSRL+RSP}$, we examine the closure statistics that result from the optimal profiles (**Figure 3B**, **Figure 4B**) where the aircraft horizontal-temporal separation is constrained (see **Section 2.4**).

The horizontal spatial and temporal aircraft separation of the first and second optimal profiles is 1.94 km–3.79 min and 11.99 km–5.97 min, respectively. The MLH of the first and second optimal profiles are at 0.59 and 0.35 km, respectively. The ATH of the first and second optimal profiles are at 4.15 and 4.00 km, respectively. The median relative bias, NMAD, and NRMSD observed in the first case study were generally worse (median relative bias = 64%, NMAD = 29%, and NRMSD = 33%), relative to the second case study (median relative bias = 42%, NMAD = 21%, and NRMSD = 28%). The r between $N_{HSRL+RSP}$ and N_{LAS} for the first and second optimal flights are 0.92 and 0.81, respectively, and both profiles are among those that have the most statistically significant correlations in the set of collocated profiles (i.e., $r > 0.80$ and p-value $\leq 10^{-9}$). In addition to these statistics **Figure 5** also provides a visual illustration of the vertically resolved N_{LAS}-$N_{HSRL+RSP}$ and column-averaged N_{LAS}-$N_{HSRL+RSP}$ closure.

To provide insight into the reasons for differences in the N_{LAS}-$N_{HSRL+RSP}$ closure, we examine the differences in the vertical profiles of RH, $r_{e,94-1130}$, α_{ext}, and LDR that correspond to the optimal profile that occurred on 26 August 2020 (**Figures 3C–F**) and the optimal profile that occurred on 28 August 2020 (**Figures 4C–F**). The RH sampled in the first optimal profile overall decreases with increasing altitude up the ATH at ~ 4 km, while the RH sampled in the second optimal profile remains relatively constant until the ATH, also at ~ 4 km. In both optimal profiles, the RH decreases sharply right above the MLH. Then, in the first optimal profile, both the α_{ext} and RH increase with altitude above the MLH to 1.5 km. In the second optimal profile, α_{ext} and RH and α_{ext} and RH are relatively constant except for a sharp increase about 1.5 km. We found that the RH is negatively correlated with $r_{e,94-1130}$ between 1 and 2 km in the first optimal profile. This behavior is in contrast to the second optimal profile, where the $r_{e,94-1130}$ increases around the spike in RH at 2 km altitude. The increase in α_{ext} might otherwise seem to indicate multiple aerosol layers sampled in both optimal profiles, but the profiles of RH and $r_{e,94-1130}$ suggest that the changes are a result of increases in RH rather than a separate unmixed layer, except in the second optimal profile around 1.5 km. At this location it is observed that LDR is elevated in the second optimal profile, and indicates the presence of non-spherical coarse-mode dust particles in the second optimal profile associated with the sharp increase in α_{ext} at 1.5 km. The dust is likely coarse-mode since there is little change in $r_{e,94-1130}$.

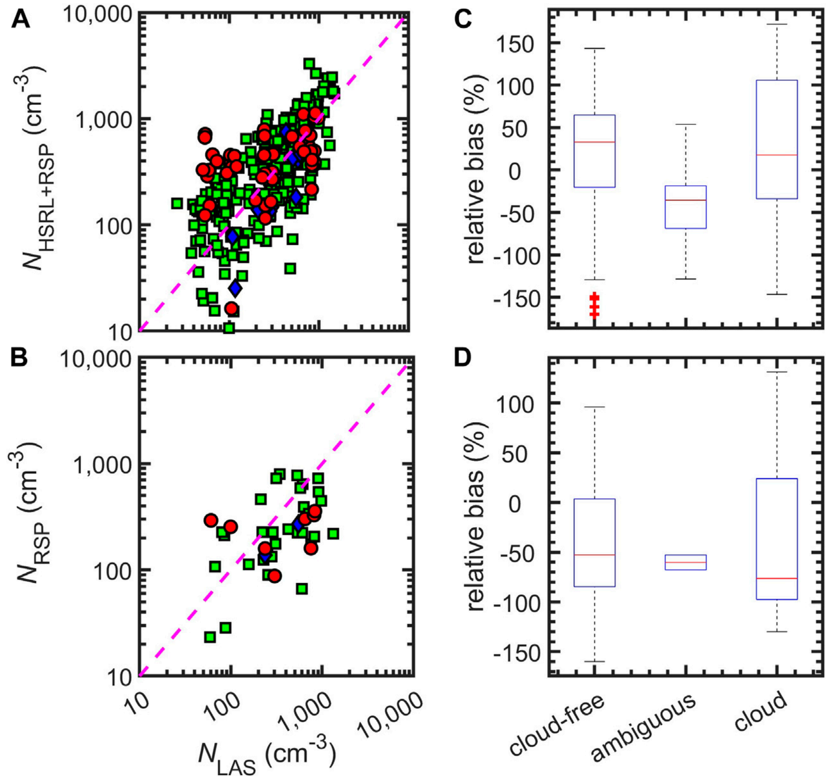

FIGURE 6 | Log-log plots of **(A)** vertically resolved $N_{\mathrm{HSRL+RSP}}$ vs. *in situ* N_{LAS} and **(B)** column-averaged N_{RSP} vs. *in situ* N_{LAS}. The collocated vertical profile data come from ACTIVATE 2020. The green squares correspond to data from vertical profiles where all *in situ* data are classified as cloud-free, blue diamonds correspond to the vertical profiles that have one or more *in situ* data point that is classified as ambiguous but no points classified as cloud, and the red circles correspond to data from vertical profiles where at least one data point was classified as cloud. The dashed-magenta line indicates the one-to-one line. Panels **(C)** and **(D)** are box plots illustrating the spread in relative bias of panel **(A)** and panel **(B)**, respectively. Data for these box plots correspond to the same categories as panels **(A)** and **(B)** (i.e., cloud-free, ambiguous, and cloud). Additional goodness of fit statistics for panels **(A)** and **(B)** are shown in Tbl. 3. Red markers on panels **(C)** or **(D)** are points that were flagged as statistical outliers. An outlier is a value that is more than 1.5 times the interquartile range away from the bottom or top of box.

Despite the presence of coarse-mode dust, the retrieval of the vertically resolved $N_{\mathrm{HSRL+RSP}}$, which is driven σ_{ext} in addition to α_{ext}, does not seem to be generally impacted except at 1.5 km where the coarse-mode dust loading peaks.

In addition to examining the profiles to identify multiple aerosol layers, the α_{ext} profile, in combination with $r_{e,94-1130}$ and RH profiles, allow us to examine the assumption of using a single fine-mode σ_{ext} to derive vertically resolved $N_{\mathrm{HSRL+RSP}}$. The narrow $r_{e,94-1130}$ range observed in the second profile suggests that there is no significant change in the fine-mode aerosol composition and size distribution. Because $r_{e,94-1130}$ can be dependent on N_{LAS}, and RH can indicate the mixing state of the atmosphere, the positive correlation between both N_{LAS} and RH with $r_{e,94-1130}$ near the surface (≤200 km altitude) seen in each profile may indicate that changes in $r_{e,94-1130}$ for near the surface are partly related to atmospheric mixing rather than composition change.

These findings from the analysis of the first optimal profile suggest that method is robust in that the correlation for $N_{\mathrm{HSRL+RSP}}$ is high despite a ~60% bias at elevated N_a and despite the separate smoke aerosol observed in the first profile. The analysis of the LDR profile suggests that non-spherical particles are not impacting the retrieval of $N_{\mathrm{HSRL+RSP}}$ significantly. In the next section, we combine data from these optimal profiles with the remaining cloud-free collocated profiles of $N_{\mathrm{HSRL+RSP}}$ and N_{LAS} to further support these findings and strengthen the validation of the $N_{\mathrm{HSRL+RSP}}$ product.

3.2 Statistical Validation

Following the initial validation with the optimal case studies, we use all collocated vertically resolved N_{LAS} data to perform a more statistically weighted validation of $N_{\mathrm{HSRL+RSP}}$ product using **Figure 6A**. Furthermore, we show that this error is generally similar to the error observed in the validation of N_{RSP} with column-averaged N_{LAS} (**Figure 6B**). Finally we examine **Figures 6C,D** and **Table 3** to demonstrate the improvements gained in validation of both vertically resolved and column-averaged N_a by removing profiles where cloud presence is detected in the column.

As noted above, there are 32 cloud-free profiles, two ambiguous profiles, and eight cloud profiles, which contain 322, 13, and 47, respectively, vertically resolved points for the comparison validation of $N_{\mathrm{HSRL+RSP}}$ and N_{LAS}. The r, median relative bias, NMAD, and NRMSD that result from the comparison of the points

TABLE 3 | Comparison statistics resulting from the comparison of vertically resolved N_{LAS} with $N_{HSRL+RSP}$ and resulting from the comparison of column-averaged N_{LAS} with N_{RSP} for the *in situ* profiles that were classified as cloud-free, ambiguous, and cloud. The statistics presented for each category are as follows (from left to right): r, *p*-value, P_{75} and P_{90} of the absolute relative bias (i.e., \|relative bias\|), NMAD, NRMSD, minimum and maximum N_{LAS} (either vertically resolved or column-averaged), and n_p.

	Conditions	r	*p*-value	|*relative bias*| (%)		NMAD	NRMSD	N_{LAS} (cm^{-3})		n_p
				P_{75}	P_{90}	(%)	(%)	min	max	
Vertically resolved	Cloud-free	0.76	$6.1 \cdot 10^{-62}$	81	106	16	24	26	1,495	322
	Ambiguous	0.71	$6.8 \cdot 10^{-3}$	69	107	28	34	109	615	13
	Cloud	0.50	$3.9 \cdot 10^{-4}$	112	145	26	33	51	983	47
Column-averaged	Cloud-free	0.35	$5.3 \cdot 10^{-2}$	90	121	21	28	59	1,327	32
	Cloud	0.36	$3.8 \cdot 10^{-1}$	1.20	131	42	47	61	832	8

contained in the cloud-free profiles are 0.76, 33%, 16%, and 24%, respectively. Additionally, this cloud-free data set resulted in a P_{90} of 106% in absolute relative bias. Data from both the ambiguous profiles and the cloud profiles resulted in worse, i.e., increases in NMAD (28% and 26%, respectively) and NRMSD (34% and 33%, respectively), relative to the NMAD and NMAD that resulted from the data cloud-free profiles. Relative to the cloud-free profile dataset, the r (0.71) and P_{90} in absolute relative bias (107%) did not change much for the ambiguous profile data set but r decreases to 0.50 and P_{90} in absolute relative bias increases to 145% for the cloud profile dataset.

Due to the limited number of column-averaged N_a points ($n_p = 2$) that are classified as ambiguous, the validation statistics for this set is not meaningful and will be omitted here. The validation statistics resulting from the comparison of the column-averaged N_a points classified as cloud-free and cloud are similar to that resulting from the vertically resolved N_a closure, with the exception of relative bias. The NMAD improves, i.e., decreases, from 42% to 21% and the NRMSD decreases from 47% to 28%. In contrast to the vertically resolved N_a, the median relative bias resulting from the column-averaged N_a comparison of the eight collocated points is −0.76, which improves to −0.53 for the 32 profiles from the column-averaged cloud-free dataset. In addition, the P_{90} in absolute relative bias of the column-averaged cloud data set is larger (131%), relative to the column-averaged cloud-free data set (121%). These findings suggest that the significantly improved performance of one set over the other, which is likely due to the fact that the retrieval of column-averaged N_a is more sensitive to deviations from ideal cloud-free conditions than the vertically resolved N_a. It is also possible that the retrieval of column-averaged N_a is more sensitive to separated aerosol layers that are possibly present. However, due to the relatively limited number of collocated points and profiles, wider application is needed to definitively conclude the main reason for the difference.

4 CONCLUSION

In this study we provide a simple and direct approach to derive vertically resolved aerosol number concentration from collocated polarimeter–lidar measurements. This method has the benefit of rapidly taking advantage of column-averaged polarimeter-derived aerosol cross section from the RSP and collocated lidar measurements of the aerosol extinction coefficient at 532 nm. Since this method only requires profiles of the extinction coefficient at 532 nm, it can be readily applied to lidar + polarimeter datasets provided that the lidar has a 532 nm high spectral resolution channel such as the NASA airborne HSRL-1 and HSRL-2 lidar, and the HSRL-1–type lidar system that will be onboard the future NASA AOS mission. We characterize the retrieval error that is observed from vertically resolved $N_{\mathrm{HSRL+RSP}}$, which is derived from column-averaged σ_{ext} from polarimeter retrievals and vertically resolved α_{ext} from HSRL-2 measurements. We demonstrate that the vertically resolved $N_{\mathrm{HSRL+RSP}}$ product has a median relative bias, P_{90} in absolute relative bias, NMAD, and NRMSD that are 0.33, 106%, 16%, and 24%, respectively. Our results also suggest that the vertically resolved $N_{\mathrm{HSRL+RSP}}$ product has similar NMAD and NRMSD as the column-averaged N_{RSP}. We demonstrate that column-averaged N_{RSP} validation is more sensitive than the vertically resolved $N_{\mathrm{HSRL+RSP}}$ to deviations from ideal conditions (e.g., cloud-free with a single aerosol layer), however elevated LDR $>10\%$ does not appear to have a significant impact on either vertically resolved or column-averaged N_a.

Although a fully combined polarimeter–lidar retrieval is expected to provide the optimal retrieval of aerosol optical and microphysical properties including aerosol number concentrations, this method provides a simple and direct approach to corroborate the results from such complex retrievals, particularly for simpler cases of single or two-layer aerosol systems. The ACTIVATE field campaign features combined polarimeter (RSP) and lidar (HSRL-2) remote sensing measurements with collocated *in situ* aerosol measurements from a second, low-flying aircraft. The ACTIVATE datasets of simultaneous remote and *in situ* measurements of aerosols in clear-sky conditions will enable us to extensively test the approach outlined here, as well as perform detailed closure studies for relating dry-wet aerosol microphysical and optical properties across passive, active, and *in situ* aerosol measurement techniques. The promise shown by the $N_{\mathrm{HSRL+RSP}}$ method can be further explored by applying the method to the rest of the ACTIVATE datasets (i.e., 2021 and 2022 flights) and to future analyses that can incorporate retrievals of the vertical structure of N_a in the atmosphere to study N_a-N_d relationships for aerosol–cloud interactions. Further application will also allow for in-depth examination of the validity of the assumption of column-averaged extinction cross sections, and the impact of scattering by coarse-mode aerosols such as sea salt aerosol on the retrieved aerosol number concentration. The hope is that the $N_{\mathrm{HSRL+RSP}}$ product can be a robust method to provide required vertical profiles of N_a for many research applications ranging from aerosol–cloud interactions to improving estimates of air quality parameters such as $PM_{2.5}$.

DATA AVAILABILITY STATEMENT

Publicly available datasets were analyzed in this study. This data can be found at: https://doi.org/10.5067/SUBORBITAL/ACTIVATE/DATA001.

AUTHOR CONTRIBUTIONS

Algorithm development: JS, SS, and BC. Data: RM, LZ, BC, CH, RF, JH, and AS. Text: all authors.

FUNDING

This work was supported through the ACTIVATE Earth Venture Suborbital-3 (EVS-3) investigation, which is funded by NASA's Earth Science Division and managed through the Earth System Science Pathfinder Program Office. Partial support was also provided by ONR grant N00014-21-1-2115.

ACKNOWLEDGMENTS

We wish to thank the pilots and aircraft maintenance personnel of NASA Langley Research Services Directorate for their work in conducting the ACTIVATE flights.

REFERENCES

Baron, P. A., and Willeke, K. (2011). *Aerosol Measurement: Principles, Techniques, and Applications*. Wiley.

Bohren, C. F., and Huffman, D. R. (1983). *Absorption and Scattering of Light by Small Particles*. Wiley.

Braun, R. A., McComiskey, A., Tselioudis, G., Tropf, D., and Sorooshian, A. (2021). Cloud, Aerosol, and Radiative Properties over the Western North Atlantic Ocean. *J. Geophys Res. Atmos.* 126, e2020JD034113. doi:10.1029/2020JD034113

Buchard, V., da Silva, A. M., Colarco, P. R., Darmenov, A., Randles, C. A., Govindaraju, R., et al. (2015). Using the Omi Aerosol Index and Absorption Aerosol Optical Depth to Evaluate the Nasa Merra Aerosol Reanalysis. *Atmos. Chem. Phys.* 15, 5743–5760. doi:10.5194/acp-15-5743-2015

Burton, S. P., Chemyakin, E., Liu, X., Knobelspiesse, K., Stamnes, S., Sawamura, P., et al. (2016). Information Content and Sensitivity of the 3<i>β</i> + 2<i>α</i> Lidar Measurement System for Aerosol Microphysical Retrievals. *Atmos. Meas. Tech.* 9, 5555–5574. doi:10.5194/amt-9-5555-2016

Burton, S. P., Ferrare, R. A., Vaughan, M. A., Omar, A. H., Rogers, R. R., Hostetler, C. A., et al. (2013). Aerosol Classification from Airborne Hsrl and Comparisons with the Calipso Vertical Feature Mask. *Atmos. Meas. Tech.* 6, 1397–1412. doi:10.5194/amt-6-1397-2013

Burton, S. P., Hostetler, C. A., Cook, A. L., Hair, J. W., Seaman, S. T., Scola, S., et al. (2018). Calibration of a High Spectral Resolution Lidar Using a Michelson Interferometer, with Data Examples from Oracles. *Appl. Opt.* 57, 6061–6075. doi:10.1364/AO.57.006061

Cairns, B., Russell, E. E., and Travis, L. D. (1999). "Research Scanning Polarimeter: Calibration and Ground-Based Measurements," in *SPIE's International Symposium on Optical Science, Engineering, and Instrumentation* (Denver, Colorado: International Society for Optics and Photonics), 186–196.

Chen, G., Ziemba, L. D., Chu, D. A., Thornhill, K. L., Schuster, G. L., Winstead, E. L., et al. (2011). Observations of Saharan Dust Microphysical and Optical Properties from the Eastern Atlantic during Namma Airborne Field Campaign. *Atmos. Chem. Phys.* 11, 723–740. doi:10.5194/acp-11-723-2011

Corral, A. F., Braun, R. A., Cairns, B., Gorooh, V. A., Liu, H., Ma, L., et al. (2021). An Overview of Atmospheric Features over the Western North Atlantic Ocean and North American East Coast - Part 1: Analysis of Aerosols, Gases, and Wet Deposition Chemistry. *J. Geophys Res. Atmos.* 126. doi:10.1029/2020JD032592

Dadashazar, H., Alipanah, M., Hilario, M. R. A., Crosbie, E., Kirschler, S., Liu, H., et al. (2021a). Aerosol Responses to Precipitation along North American Air Trajectories Arriving at bermuda. *Atmos. Chem. Phys.* 21, 16121–16141. doi:10.5194/acp-21-16121-2021

Dadashazar, H., Painemal, D., Alipanah, M., Brunke, M., Chellappan, S., Corral, A. F., et al. (2021b). Cloud Drop Number Concentrations over the Western North Atlantic Ocean: Seasonal Cycle, Aerosol Interrelationships, and Other Influential Factors. *Atmos. Chem. Phys.* 21, 10499–10526. doi:10.5194/acp-21-10499-2021

Dadashazar, H., Wang, Z., Crosbie, E., Brunke, M., Zeng, X., Jonsson, H., et al. (2017). Relationships between Giant Sea Salt Particles and Clouds Inferred from Aircraft Physicochemical Data. *J. Geophys. Res. Atmos.* 122, 3421–3434. doi:10.1002/2016JD026019

Diskin, G. S., Podolske, J. R., Sachse, G. W., and Slate, T. A. (2002). "Open-path Airborne Tunable Diode Laser Hygrometer," in *Diode Lasers and Applications in Atmospheric Sensing*. Editor A. Fried (Seattle, Washington D.C.: International Society for Optics and Photonics), 4817, 196–204. doi:10.1117/12.453736

Feingold, G. (2003). Modeling of the First Indirect Effect: Analysis of Measurement Requirements. *Geophys. Res. Lett.* 30. doi:10.1029/2003GL017967

Fernald, F. G. (1984). Analysis of Atmospheric Lidar Observations: Some Comments. *Appl. Opt.* 23, 652–653. doi:10.1364/ao.23.000652

Georgoulias, A. K., Marinou, E., Tsekeri, A., Proestakis, E., Akritidis, D., Alexandri, G., et al. (2020). A First Case Study of Ccn Concentrations from Spaceborne Lidar Observations. *Remote Sens.* 12, 1557. doi:10.3390/rs12101557

Grosvenor, D. P., Sourdeval, O., Zuidema, P., Ackerman, A., Alexandrov, M. D., Bennartz, R., et al. (2018). Remote Sensing of Droplet Number Concentration in Warm Clouds: A Review of the Current State of Knowledge and Perspectives. *Rev. Geophys.* 56, 409–453. doi:10.1029/2017RG000593

Gryspeerdt, E., Quaas, J., Ferrachat, S., Gettelman, A., Ghan, S., Lohmann, U., et al. (2017). Constraining the Instantaneous Aerosol Influence on Cloud Albedo. *Proc. Natl. Acad. Sci. U.S.A.* 114, 4899–4904. doi:10.1073/pnas.1617765114

Hair, J. W., Hostetler, C. A., Cook, A. L., Harper, D. B., Ferrare, R. A., Mack, T. L., et al. (2008). Airborne High Spectral Resolution Lidar for Profiling Aerosol Optical Properties. *Appl. Opt.* 47, 6734–6752. doi:10.1364/ao.47.006734

Hammer, M. S., Martin, R. V., van Donkelaar, A., Buchard, V., Torres, O., Ridley, D. A., et al. (2016). Interpreting the Ultraviolet Aerosol Index Observed with the Omi Satellite Instrument to Understand Absorption by Organic Aerosols: Implications for Atmospheric Oxidation and Direct Radiative Effects. *Atmos. Chem. Phys.* 16, 2507–2523. doi:10.5194/acp-16-2507-2016

Hasekamp, O. P., Gryspeerdt, E., and Quaas, J. (2019). Analysis of Polarimetric Satellite Measurements Suggests Stronger Cooling Due to Aerosol-Cloud Interactions. *Nat. Commun.* 10, 5405. doi:10.1038/s41467-019-13372-2

Knobelspiesse, K., Cairns, B., Ottaviani, M., Ferrare, R., Hair, J., Hostetler, C., et al. (2011). Combined Retrievals of Boreal Forest Fire Aerosol Properties with a

Polarimeter and Lidar. *Atmos. Chem. Phys.* 11, 7045–7067. doi:10.5194/acp-11-7045-2011

MacDonald, A. B., Dadashazar, H., Chuang, P. Y., Crosbie, E., Wang, H., Wang, Z., et al. (2018). Characteristic Vertical Profiles of Cloud Water Composition in Marine Stratocumulus Clouds and Relationships with Precipitation. *J. Geophys. Res. Atmos.* 123, 3704–3723. doi:10.1002/2017JD027900

Mardi, A. H., Dadashazar, H., Painemal, D., Shingler, T., Seaman, S. T., Fenn, M. A., et al. (2021). Biomass Burning over the united states East Coast and Western North Atlantic Ocean: Implications for Clouds and Air Quality. *JGR Atmos.* 126, e2021JD034916. doi:10.1029/2021JD034916

McNaughton, C. S., Clarke, A. D., Howell, S. G., Pinkerton, M., Anderson, B., Thornhill, L., et al. (2007). Results from the Dc-8 Inlet Characterization Experiment (Dice): Airborne versus Surface Sampling of Mineral Dust and Sea Salt Aerosols. *Aerosol Sci. Technol.* 41, 136–159. doi:10.1080/02786820601118406

Müller, D., Chemyakin, E., Kolgotin, A., Ferrare, R. A., Hostetler, C. A., and Romanov, A. (2019). Automated, Unsupervised Inversion of Multiwavelength Lidar Data with Tiara: Assessment of Retrieval Performance of Microphysical Parameters Using Simulated Data. *Appl. Opt.* 58, 4981–5008. doi:10.1364/AO.58.004981

Murphy, D. M., Froyd, K. D., Bian, H., Brock, C. A., Dibb, J. E., DiGangi, J. P., et al. (2019). The Distribution of Sea-Salt Aerosol in the Global Troposphere. *Atmos. Chem. Phys.* 19, 4093–4104. doi:10.5194/acp-19-4093-2019

Painemal, D., Corral, A. F., Sorooshian, A., Brunke, M. A., Chellappan, S., Afzali Gorooh, V., et al. (2021). An Overview of Atmospheric Features over the Western North Atlantic Ocean and North American East Coast-Part 2: Circulation, Boundary Layer, and Clouds. *Geophys Res. Atmos.* 126. doi:10.1029/2020JD033423

Quinn, P. K., Bates, T. S., Coffman, D. J., Upchurch, L., Johnson, J. E., Moore, R., et al. (2019). Seasonal Variations in Western North Atlantic Remote Marine Aerosol Properties. *J. Geophys. Res. Atmos.* 124, 14240–14261. doi:10.1029/2019JD031740

Sawamura, P., Moore, R. H., Burton, S. P., Chemyakin, E., Müller, D., Kolgotin, A., et al. (2017). Hsrl-2 Aerosol Optical Measurements and Microphysical Retrievals vs. Airborne *In Situ* Measurements during Discover-Aq 2013: an Intercomparison Study. *Atmos. Chem. Phys.* 17, 7229–7243. doi:10.5194/acp-17-7229-2017

Scarino, A. J., Obland, M. D., Fast, J. D., Burton, S. P., Ferrare, R. A., Hostetler, C. A., et al. (2014). Comparison of Mixed Layer Heights from Airborne High Spectral Resolution Lidar, Ground-Based Measurements, and the Wrf-Chem Model during Calnex and Cares. *Atmos. Chem. Phys.* 14, 5547–5560. doi:10.5194/acp-14-5547-2014

Shingler, T., Dey, S., Sorooshian, A., Brechtel, F. J., Wang, Z., Metcalf, A., et al. (2012). Characterisation and Airborne Deployment of a New Counterflow Virtual Impactor Inlet. *Atmos. Meas. Tech.* 5, 1259–1269. doi:10.5194/amt-5-1259-2012

Shinozuka, Y., Clarke, A. D., Nenes, A., Jefferson, A., Wood, R., McNaughton, C. S., et al. (2015). The Relationship between Cloud Condensation Nuclei (Ccn) Concentration and Light Extinction of Dried Particles: Indications of Underlying Aerosol Processes and Implications for Satellite-Based Ccn Estimates. *Atmos. Chem. Phys.* 15, 7585–7604. doi:10.5194/acp-15-7585-2015

Sinclair, K., van Diedenhoven, B., Cairns, B., Alexandrov, M., Moore, R., Crosbie, E., et al. (2019). Polarimetric Retrievals of Cloud Droplet Number Concentrations. *Remote Sens. Environ.* 228, 227–240. doi:10.1016/j.rse.2019.04.008

Sorooshian, A., Corral, A. F., Braun, R. A., Cairns, B., Crosbie, E., Ferrare, R., et al. (2020). Atmospheric Research over the Western North Atlantic Ocean Region and North American East Coast: A Review of Past Work and Challenges Ahead. *J. Geophys Res. Atmos.* 125, e2019JD031626. doi:10.1029/2019JD031626

Sorooshian, A., Anderson, B., Bauer, S. E., Braun, R. A., Cairns, B., Crosbie, E., et al. (2019). Aerosol-Cloud-Meteorology Interaction Airborne Field Investigations: Using Lessons Learned from the U.S. West Coast in the Design of ACTIVATE off the U.S. East Coast. *Bull. Am. Meteorological Soc.* 100, 1511–1528. doi:10.1175/BAMS-D-18-0100.1

Sorooshian, A., Atkinson, J., Ferrare, R., Hair, J., and Ziemba, L. (2021). Taking Flight to Study Clouds and Climate. *EOS* 102. doi:10.1029/2021EO158570

Stamnes, S., Hostetler, C., Ferrare, R., Burton, S., Liu, X., Hair, J., et al. (2018). Simultaneous Polarimeter Retrievals of Microphysical Aerosol and Ocean Color Parameters from the "MAPP" Algorithm with Comparison to High-Spectral-Resolution Lidar Aerosol and Ocean Products. *Appl. Opt.* 57, 2394–2413. doi:10.1364/ao.57.002394

Thornhill, K. L., Anderson, B. E., Barrick, J. D. W., Bagwell, D. R., Friesen, R., and Lenschow, D. H. (2003). Air Motion Intercomparison Flights during Transport and Chemical Evolution in the Pacific (Trace-p)/ace-asia. *J. Geophys. Res.* 108. doi:10.1029/2002JD003108

Wang, Z., Sorooshian, A., Prabhakar, G., Coggon, M. M., and Jonsson, H. H. (2014). Impact of Emissions from Shipping, Land, and the Ocean on Stratocumulus Cloud Water Elemental Composition during the 2011 E-Peace Field Campaign. *Atmos. Environ.* 89, 570–580. doi:10.1016/j.atmosenv.2014.01.020

Wu, L., Hasekamp, O., van Diedenhoven, B., Cairns, B., Yorks, J. E., and Chowdhary, J. (2016). Passive Remote Sensing of Aerosol Layer Height Using Near-Uv Multiangle Polarization Measurements. *Geophys. Res. Lett.* 43, 8783–8790. doi:10.1002/2016GL069848

Yin, J.-F., Wang, D.-H., Zhai, G.-Q., and Xu, H.-B. (2014). An Investigation into the Relationship between Liquid Water Content and Cloud Number Concentration in the Stratiform Clouds over North china. *Atmos. Res.* 139, 137–143. doi:10.1016/j.atmosres.2013.12.004

Conflict of Interest: Author EC is employed by Science Systems and Applications, Inc.

The remaining authors declare that the research was conducted in the absence of any commercial or financial relationships that could be construed as a potential conflict of interest.